

Fluorination of Star-Shaped Cyclopenta[2,1-b;3,4-b'] dithiophene Derivatives and Its Application as Hole-Transporting Materials in Scalable Perovskite Solar Cell Fabrication by Bar Coating

Gizachew Belay Adugna, Kun-Mu Lee,* Hsiao-Chi Hsieh,* Shih-I Lu,* Chia-Hui Lin, Yu-Chien Hsieh, June Hung Yang, Jian-Ming Chiu, Yun-Shuo Liu, Chih-Wei Hu, Wei-Hao Chiu, Sie-Rong Li, Kang-Ling Liau, Yu-Tai Tao, and Yan-Duo Lin*

In this study, three novel star-shaped small molecules HYC-oF, HYC-mF, and HYC-H are designed and synthesized and are applied in perovskite solar cells (PSCs) as efficient hole-transporting materials (HTMs). Compared with non-fluorinated HYC-H, F-substituted analogs HYC-oF and HYC-mF exhibited enhanced hole mobility, suitable energy level alignment, improved interfacial contact and hole extraction/transport capability, better passivation effect, as well as increased hydrophobicity. PSC fabrication by spin-coating this series of HYC-oF, HYC-mF, and HYC-H molecules on a bar-coated perovskite layer yielded PCEs values of 19.64%, 18.38%, and 16.98%, respectively. In order to realize a fully scalable PSC preparation process, sequential coating of HYC-oF layer on perovskite layer all by thermal-assisted bar-coating (TABC) method was carried out on $10 \times 10 \text{ cm}^2$ area. The TABC-based HYC-oF layer had a compact and uniform morphology with full surface coverage on the TABC-based perovskite film. Under optimized condition, the PSCs fabricated from such film exhibited a PCE of 18.49% as compared with a lower power conversion efficiency (PCE) of 17.51% from the reference cell using TABC-based spiro-OMeTAD. This work demonstrates the potential of fluorinated star-shaped cyclopenta[2,1-b;3,4-b'] dithiophene (CPDT)-based molecule as HTM for achieving efficient PSC in both small and large scale.


1. Introduction

In the past decade, hybrid metal-halide perovskite solar cells (PSCs) have attracted enormous attention due to their ease of fabrication, excellent optoelectronic properties, and incredible power conversion efficiency (PCE) growth from 3.8% to 26.1% over recent years.^[1] However, most high-performance *n-i-p* PSCs used 2,2',7,7'-tetrakis[*N,N*-di(4-methoxyphenyl)amino]-9,9'-spirobifluorene (spiro-OMeTAD) as hole-transporting material (HTM) on the perovskite layer. Nevertheless, this material suffers from complex preparation processes and immensely high price. In this regard, it is crucial to design and synthesize low-cost HTMs with a remarkable photovoltaic performance to address these issues. In an attempt to replace spiro-OMeTAD, many new molecules have been synthesized with thiophene-fused molecular backbone such as dithieno[3,2-b:2',3'-d]pyrrole (DTP), tetrathienopyrrole (TTTP), benzo[1,2-b:4,5-b']dithiophene (BDT), benzo[1,2-b:3,4-b':5,6-b'']trithiophene (BT),^[2]

and so forth, where sulfur atoms are believed to be able to passivate perovskite surface defects by coordinating Pb^{2+} vacancies,

G. B. Adugna, S.-I. Lu, C.-H. Lin, Y.-C. Hsieh, J. H. Yang, Y.-S. Liu, Y.-D. Lin
Department of Chemistry
Soochow University
Taipei 11102, Taiwan
E-mail: shih_i_lu@hotmail.com; ydlin@scu.edu.tw

G. B. Adugna, S.-R. Li, Y.-T. Tao
Institute of Chemistry
Academia Sinica
Taipei 115024, Taiwan

 The ORCID identification number(s) for the author(s) of this article can be found under <https://doi.org/10.1002/solr.202300988>.

DOI: 10.1002/solr.202300988

K.-M. Lee, W.-H. Chiu
Department of Chemical and Materials Engineering
Chang Gung University
Taoyuan 33302, Taiwan
E-mail: kmlee@mail.cgu.edu.tw

K.-M. Lee
Division of Neonatology, Department of Pediatrics
Chang Gung Memorial Hospital
Linkou Taoyuan 33305, Taiwan

K.-M. Lee, W.-H. Chiu
Center for Sustainability and Energy Technologies
Chang Gung University
Taoyuan 33302, Taiwan

which will help to suppress non-radiative losses at the perovskite/HTM interface and improve the device performance.^[3]

Among the reported thiophene-fused HTMs, the cyclopenta[2,1-b;3,4-b']dithiophene (CPDT) has also been employed as a central core to construct the HTMs for highly efficient PSCs. Previously, Michael Grätzel et al. and Guoli Tu et al. independently reported two HTMs based on the spiro-CPDT central core for *n-i-p* PSCs that attained the PCEs of 13.4% and 10.4%, respectively. In 2016, Mohammad Khaja Nazeeruddin et al. constructed an HTM featuring a [cyclopenta[2,1-b:3,4-b']dithiophene-4,9'-fluorene] central core, and the *n-i-p* PSCs yielded a remarkable PCE of 20.2%. In 2023, Zhou et al. synthesized a two-dimensional HTM with CPDT as core structure for *p-i-n* PSCs, achieving a maximum efficiency of 20.77%.^[4] Recently, our group developed a series of HTMs based on CPDT central scaffold and fabricated high efficiency devices with PCEs in the range of 17.71%–23.59%.^[5] These great progresses indicated the incorporation of the CPDT moiety into HTM molecules is a promising strategy for fabricating highly efficient PSCs.

In addition, fluorination of molecular backbone has been reported to be a strategy for improving optoelectronic properties, charge mobility, film morphology, and increasing hydrophobicity.^[6] Therefore, fluorinated HTMs are widely used to enhance photovoltaic performance and device stability of PSCs. For instance, in 2017 Zhu et al. reported a fluorinated HTM composed of benzothiadiazole (BT) for PSCs with a PCE of 18.54%. In 2020, Li and co-workers introduced the fluorinated benzo[1,2-b:4,5-b']dithiophene as the core to develop a new HTM (**H2**), which showed a better morphology and gave a high PCE of 18.69% in PSCs application.^[7] In the same year, Jeong et al. reported a series of fluorinated spiro-OMeTAD analogues, **spiro-mF** and **spiro-oF**, with a tightly stacked molecular arrangement, as HTM and achieved an excellent PCE over 24%.^[8] Very recently, we demonstrated that the pentafulvalene-fused HTMs with fluorinated triphenylamine (TPA) motifs as donor succeeded in increasing hole-transport mobility and improving the film formation, and ultimately enhancing photovoltaic performance while compared with non-fluorinated one.^[5h]

K.-M. Lee
College of Environment and Resources
Ming Chi University of Technology
New Taipei City 24301, Taiwan

H.-C. Hsieh
Department of Applied Materials Science and Technology
Minghsin University of Science and Technology
Hsinchu 30401, Taiwan
E-mail: hchsieh@must.edu.tw

J.-M. Chiu
Department of Chemical Engineering
National Taiwan University of Science and Technology
Taipei 106335, Taiwan

C.-W. Hu
National Synchrotron Radiation Research Center
Hsinchu 300092, Taiwan

K.-L. Liu
Department of Chemistry
National Central University
Taoyuan 32001, Taiwan

Obviously, the fluorination of molecular backbones is a good strategy for realizing highly efficient PSCs. Although these promising achievements have been made for F-substituted HTMs, the HTM films were fabricated using spin-coating method in small-area PSCs. Nevertheless, the conventional spin-coating method is difficult to realize a large-area perovskite coating.

Various scalable coating-techniques, such as bar-coating, blade-coating, slot-die coating, spray-coating, and thermal evaporation, were proposed for large-area films.^[9] For scalable fabrication of perovskite films, bar-coating method has been employed for coating the perovskite solution on large-area substrate and shown impressive results, indicating that the bar coating is one feasible method for mass production.^[10] So far, to the best of our knowledge, for most of efficient bar-coated PSCs, the HTM, such as spiro-OMeTAD was prepared onto bar-coated perovskite films by the spin-coating process, which is not a suitable method for preparing large-area films.^[11]

Based on the discussions above, it is highly desirable to develop new fluorinated HTMs as alternatives to the expensive spiro-OMeTAD material, and use it in large-area PSCs. Thus, in this work we designed and synthesized three star-shaped HTMs, denoted as **HYC-oF**, **HYC-mF**, and **HYC-H**, which are composed of CPDT moiety as a building block featuring fluorinated and nonfluorinated TPA as the donor (**Figure 1**) and demonstrated their use in a scalable PSC fabrication, with a structure of FTO/c-TiO₂/mp-TiO₂/CH₃NH₃PbI₃/HTM/Ag, where both the perovskite film and the HTM layer were prepared by the thermal-assisted bar-coating (TABC) technique. We first investigated the spin-coated HTMs film on the TABC-based large-area perovskite layer. The PSCs containing the novel **HYC** series as HTMs were successfully prepared, with the fluorinated **HYC-oF** and **HYC-mF** as HTMs exhibiting the higher PCEs of 19.64% and 18.38%, respectively and improved device stability compare to the non-fluorinated counterpart **HYC-H** and the control of spiro-OMeTAD-based devices, where the PCEs of 16.98% and 19.02%, were obtained respectively. The fluorinated HTMs exhibited a well-matched energy level, a higher hole mobility, a better film morphology, and increased hydrophobicity as well as passivation effect. Furthermore, we successfully demonstrated that **HYC-oF** can be coated sequentially on the perovskite layer over a large-area substrate (10 × 10 cm²) by TABC method. The **HYC-oF**-based device made from these films exhibited a remarkable PCE of 18.49%, which was higher than the control device with spiro-OMeTAD (17.51%) prepared in the same way. The present work demonstrates the great potential of fluorinated CPDT derivatives to construct highly efficient large-area PSCs in the future.

2. Results and Discussion

The synthetic routes of the three new HTMs, **HYC-oF**, **HYC-mF**, and **HYC-H**, are depicted in **Scheme 1**. The synthesized products are fully characterized by ¹H NMR spectra, ¹³C NMR spectra, ¹⁹F NMR spectra and HRMS (**Figure S1–S19**, Supporting Information). Compounds **1–3**^[5h] were coupled with 2,6-dibromo-4H-cyclopenta[2,1-b:3,4-b']dithiophene (**4**) through a Suzuki coupling reaction to give compounds **5–7**.^[5a] Subsequently, the final products **HYC-oF**, **HYC-mF**, and

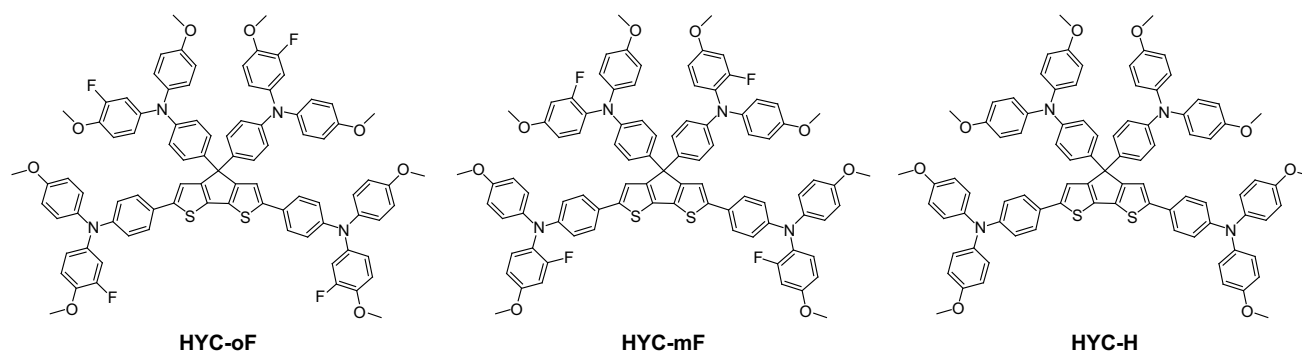
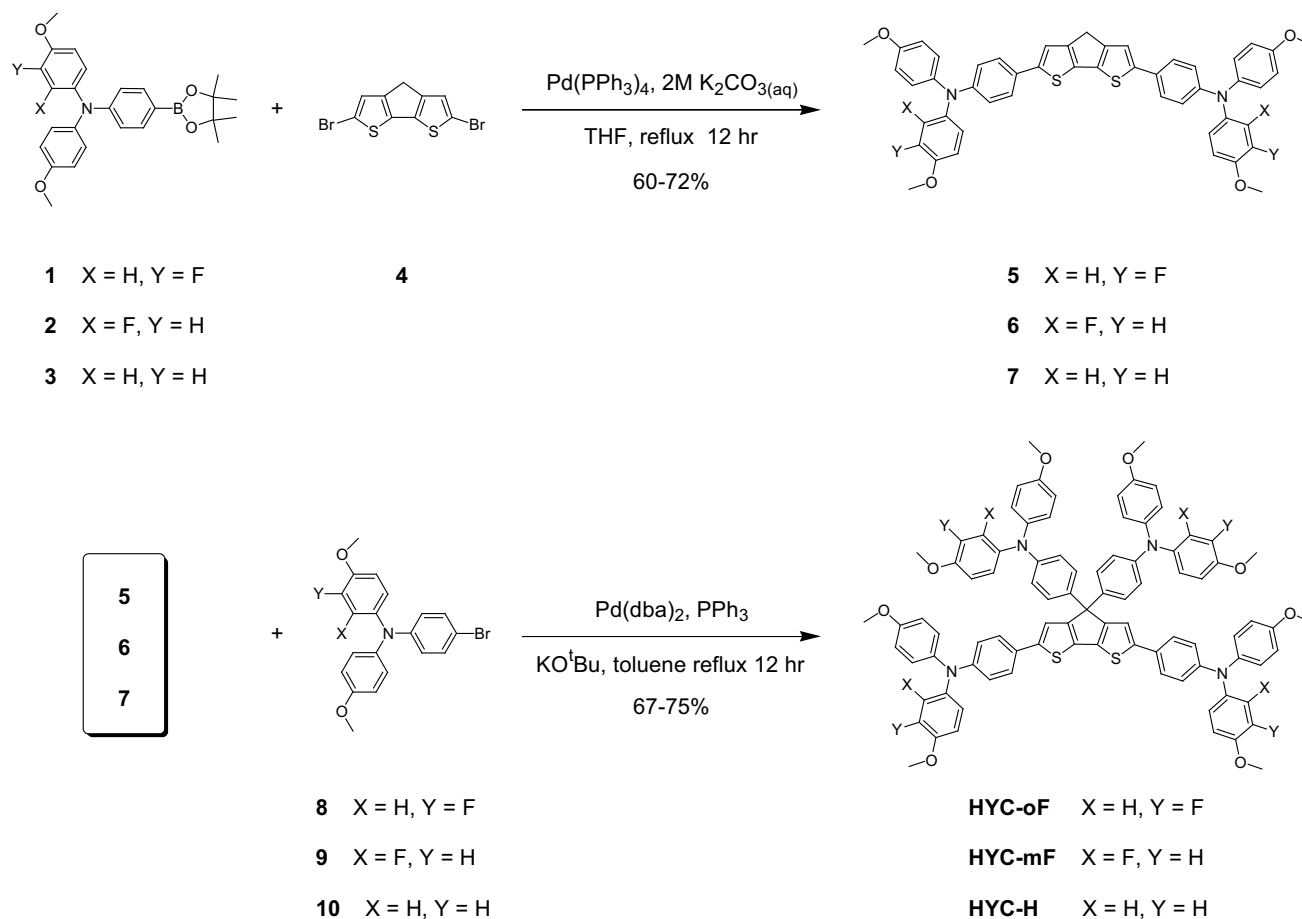


Figure 1. Chemical structures of **HYC-oF**, **HYC-mF**, and **HYC-H**.



Scheme 1. Synthetic procedures for **HYC-oF**, **HYC-mF**, and **HYC-H**.

HYC-H were obtained by the Pd-catalyzed C–H bond activation of compounds **5–7**, followed by coupling with the intermediates **8–10**. In this process, the material cost of **HYC-oF**, **HYC-mF**, and **HYC-H** were evaluated. As shown in Table S1–S14, Supporting Information, the costs of **HYC-oF**, **HYC-mF**, and **HYC-H** are calculated to be \$92.72, \$95.81, and \$35.87 g⁻¹, respectively, which are lower than that of spiro-OMeTAD (\$170–\$475 g⁻¹).^[12,13]

The thermal properties of **HYC-oF**, **HYC-mF**, and **HYC-H** were evaluated by thermogravimetric analysis (TGA) and differential scanning calorimetry (DSC) measurements. As shown in Figure S20, Supporting Information, **HYC** series exhibited good thermal stability with the decomposition temperatures (T_d , the temperature with 5% weight-loss) over 380 °C, demonstrating that the **HYC** series HTMs are thermally stable for application in PSCs. Meanwhile, the DSC curves exhibited a glass transition

temperature (T_g) of 148, 147, and 141 °C for **HYC-oF**, **HYC-mF**, and **HYC-H**, respectively, revealing the stability of the amorphous films of **HYC** derivatives. Furthermore, the powder X-ray diffraction (PXRD) was performed on the thin films of **HYC-oF**, **HYC-mF**, and **HYC-H** (Figure S21, Supporting Information). The PXRD patterns of **HYC** series show broad characteristics bands, indicating that the new HTMs tend to be amorphous.

Subsequently, density functional theory (DFT) calculations at B3LYP/6-31G (d,p) level were performed to get insight into the optimized molecular geometries and frontier molecular orbitals distribution of **HYC** series. As shown in **Figure 2**, the highest occupied molecular orbitals (HOMOs) spread over the whole molecule, from the CPDT core to the triphenylamine moieties, whereas the lowest unoccupied molecular orbitals (LUMOs) more localizes in the CPDT part. Moreover, the HOMO and LUMO energy levels of **HYC-oF**, **HYC-mF**, and **HYC-H** were

estimated by DFT calculations to be $-4.34/-1.44$, $-4.22/-1.21$, and $-4.19/-1.32$ eV, respectively (Figure 2a). It was found that the HOMO energy levels of fluorinated **HYC-oF** and **HYC-mF** were lower than that of non-fluorinated one (**HYC-H**), presumably owing to the strong electron-withdrawing nature of fluorine atoms, which is beneficial to higher open-circuit voltage (V_{oc}) values and thus PCEs. The optimized geometries of the three HTMs are displayed in Figure 2b. The **HYC-oF**, **HYC-mF**, and **HYC-H** display a similarly highly twisted configuration due to the orthogonal arrangement of two triphenylamine moieties on the central CPDT unit, which is favorable to their solubility in organic solvents and formation of high-quality films. Furthermore, the calculated dipole moments of **HYC-oF** (5.53 D) and **HYC-mF** (5.26 D) are larger than that of **HYC-H** (3.15 D), presumably due to the intrinsic D–A characteristics, suggesting a stronger molecular interaction within these HTMs as well as with the positively charged defects of the perovskite. Therefore, a better passivation effect may be expected.

The UV-Vis absorption spectra and photoluminescence spectra of **HYC-oF**, **HYC-mF**, and **HYC-H** were measured in THF solution to investigate their optical properties. The corresponding parameters are collected in **Table 1**. As shown in **Figure 3a**, the three new HTMs all showed two prominent absorption bands at around 300 and 440–450 nm, respectively, with the lower energy bands attributable to intramolecular charge transfer (ICT) transitions from the arylamine to the central CPDT moiety, as evidenced by the DFT calculations results above. It was found that the absorption peak in the longer wavelength region of fluorinated HTMs (**HYC-oF** and **HYC-mF**) displayed a slight blue-shift relative to that of non-fluorinated counterpart (**HYC-H**). It can be ascribed to the strong electronegativity of fluorine atoms on the aromatic rings.^[7a] Furthermore, the time-dependent DFT (TD-DFT) calculation was carried out to elucidate the origin of the two broad absorption bands. As illustrated in Figure S22, Supporting Information, the simulated spectra suggest the absorption bands of **HYC** series in the short wavelength region (300–380 nm) can be ascribed to the $\pi-\pi^*$ transition, and the absorption peaks in the long wavelength region (400–550 nm) can be assigned to the ICT character from triphenylamine blocks to the central CPDT core. The shape of simulated UV-Vis spectra for **HYC-oF**, **HYC-mF**, and **HYC-H** are in good agreement with the experimental results (Figure 3a). For the photoluminescent spectra, the maximum emission peaks are located at 504, 498, and 507 nm for **HYC-oF**, **HYC-mF**, and **HYC-H**, respectively. Obviously, the fluorinated HTMs (**HYC-oF** and **HYC-mF**)

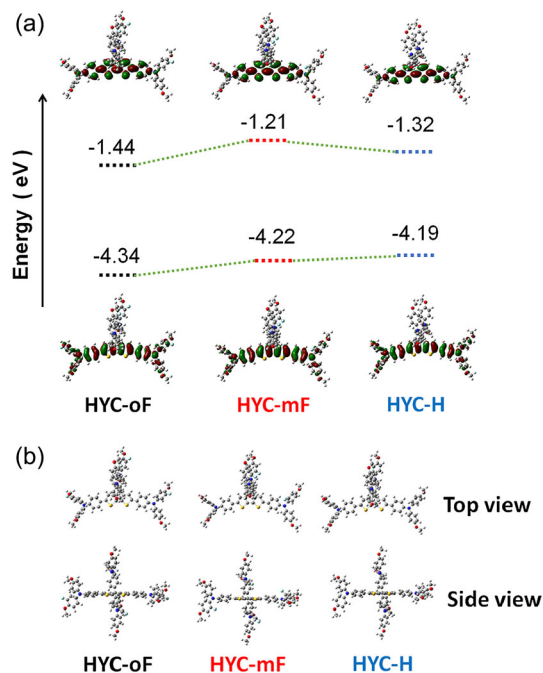


Figure 2. a) HOMO and LUMO distributions and the calculated energy levels of **HYC-oF**, **HYC-mF**, and **HYC-H** at the B3LYP/6-31 G (d,p) level. b) Top view and side view of DFT optimized molecular configurations.

Table 1. Photophysical, electrochemical, and thermal data of **HYC-oF**, **HYC-mF**, **HYC-H** and spiro-OMeTAD.

HTM	λ_{abs} [nm] ($\epsilon \times 10^{-4}/[M]^{-1} [cm]^{-1}$) ^{a)}	λ_{fl} [nm] ^{a)}	E_{HOMO} [eV] ^{b)}	$E_{0,0}$ [eV] ^{c)}	E_{LUMO} [eV] ^{d)}	E_{HOMO} [eV] ^{e)}	$E_{0,0}$ [eV] ^{e)}	E_{LUMO} [eV] ^{e)}	T_g [°C] ^{f)}	T_d [°C] ^{g)}
HYC-oF	440 (5.90)	504	-5.26	2.56	-2.70	-4.34	2.90	-1.44	148	381
HYC-mF	435 (6.09)	497	-5.20	2.59	-2.61	-4.22	3.01	-1.21	147	432
HYC-H	443 (6.21)	508	-5.19	2.65	-2.54	-4.19	2.87	-1.32	141	424
spiro-OMeTAD	389 (18.4)	428	-5.15	3.02	-2.13	-4.21	3.60	-0.61	121 ^{h)}	422 ^{h)}

^{a)}Maxima of the absorption and fluorescence bands in THF solution; ^{b)}Determined by differential pulse voltammetry (DPV); ^{c)}The value of $E_{0,0}$ obtained from the intersection of normalized absorption and photoluminescence spectra; ^{d)}Energy of the LUMO levels of the compounds estimated by $E_{HOMO} + E_{0,0}$; ^{e)}Values calculated at DFT/B3LYP/6-31 G(d,p) level; ^{f)}Glass transition (T_g) and decomposition (T_d) temperatures observed from TGA and DSC, respectively; ^{g)}Data reported in reference.^[15]

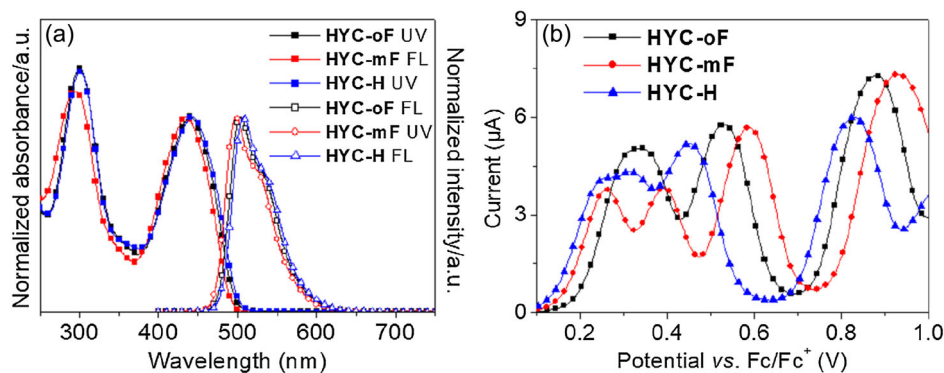


Figure 3. a) Normalized absorption and photoluminescence spectra of **HYC** series in THF solution. b) Differential pulsed voltammetry (DPV) curves of **HYC** series in THF solution.

exhibited blue shift of emission than non-fluorinated one (**HYC-H**), which might be ascribed to the electron-withdrawing inductive effect of the fluorine atoms on the aromatic ring. The optical energy band gaps (E_g) of **HYC-oF**, **HYC-mF**, and **HYC-H** were calculated to be 2.56, 2.59, and 2.65 eV, respectively from the intersection of normalized absorption and photoluminescence spectra.

The electrochemical properties of three HTMs were investigated by means of cyclic voltammetry (CV) (Figure S23, Supporting Information) and differential pulse voltammetry (DPV) measurements in THF solution using ferrocene/ferrocenium (Fc/Fc^+) as the internal standard, and the detailed electrochemical data are shown in Table 1. As shown in Figure 3b, the observed HOMO energy levels of **HYC-oF**, **HYC-mF**, and **HYC-H** are at -5.26 , -5.20 , and -5.19 eV, respectively, whose trend agrees well with the DFT calculation results. Furthermore, the HOMO levels of **HYC** series are higher than the valence band of perovskite (-5.43 eV), which ensures efficient hole transfer from the perovskite to HTMs. Meanwhile, the LUMO energy levels of three HTMs are at -2.70 , -2.61 , and -2.54 eV, respectively, which are above the conduction band of the perovskite, ensuring an effective electron-blocking ability. Compared with **HYC-H**, the **HYC-oF** and **HYC-mF** with additional fluorine atoms on the phenyl groups as the electron donor have lower HOMO levels, which match well with the valence band of perovskite. It suggests that the energy loss of hole extraction from fluorinated HTMs is lower than that from non-fluorinated analog, which is beneficial to achieving higher V_{oc} values.

The hole-transporting properties for the **HYC** series and spiro-OMeTAD were investigated through the space-charge-limited current (SCLC) model (Figure S24, Supporting Information). The hole mobility of **HYC-oF**, **HYC-mF**, **HYC-H**, and spiro-OMeTAD were extracted to be 6.57×10^{-4} , 2.09×10^{-4} , 2.94×10^{-5} and $8.06 \times 10^{-5} \text{ cm}^2 \text{ V}^{-1} \text{ s}^{-1}$, respectively. Fluorinated HTMs of **HYC-oF** and **HYC-mF** exhibited relatively higher hole mobilities as compared with the non-fluorinated counterpart **HYC-H**. These results may suggest the introduction of fluorine atom helps to reduce intermolecular distance and facilitate hole hopping between molecules and thus enhance hole mobility.^[7] Similar phenomenon has been observed in our previous fluorinated HTMs.^[5h] To further explore the hole

transporting behavior of **HYC** series, the intermolecular interaction and packing information were estimated by DFT calculations (Figure S25, Supporting Information). The intermolecular binding energies were calculated to be -114.65 , -110.80 , and $-107.47 \text{ kcal mol}^{-1}$ for **HYC-oF**, **HYC-mF**, and **HYC-H**, respectively. These results suggest that **HYC-oF** forms more compact molecular packing, and thus has increased hole transport capability and promote the hole mobility in PSCs, which is in good agreement with the hole mobility measured by SCLC method.

The steady-state photoluminescence (PL) and time-resolved photoluminescence (TRPL) were also measured to gain insight into the hole extraction and collection capability from perovskite layer to the HTM layer and the results are shown in Figure 4. Compare with bare pristine perovskite film, the PL emission was significantly quenched by 98.2%, 96.6%, 92.4%, and 95.6% after the perovskite films were deposited over **HYC-oF**, **HYC-mF**, **HYC-H**, and spiro-OMeTAD, respectively. This indicates more efficient hole extraction by the fluorinated HTM layers (**HYC-oF** and **HYC-mF**) relative to the non-fluorinated analog (**HYC-H**). Moreover, the TRPL spectra were fitted by the bi-exponential model. As illustrated in Figure 4b, the average decay lifetimes (τ_{avg}) of bilayered **HYC-oF**/perovskite ($\tau_{avg} = 7.86 \text{ ns}$) and **HYC-mF**/perovskite ($\tau_{avg} = 19.59 \text{ ns}$) samples are shorter than that of **HYC-H**/perovskite sample ($\tau_{avg} = 20.82 \text{ ns}$) (Table S18, Supporting Information), implying that a more efficient charge transfer at the interface of perovskite/fluorinated HTM layers.

The quality of perovskite film and the coverage of HTM films deposited on top are not only crucial to interfacial charge transfer, but also vital in determining the photovoltaic performance of PSCs. Scanning electron microscopy (SEM) was firstly used to examine the morphology of the perovskite film fabricated by TABC method (Figure 5a). It can be seen that besides the clear domain boundaries, a good morphology of perovskite films without voids and pinholes was obtained. Then the surface morphologies of **HYC-oF**, **HYC-mF**, **HYC-H**, and spiro-OMeTAD spin-coated on top of perovskite layer were examined. As shown in Figure 5b–e, **HYC** series gave smooth, dense, and homogeneous morphology with full surface coverage on the perovskite layer. The wider domain boundaries from the large crystalline domains

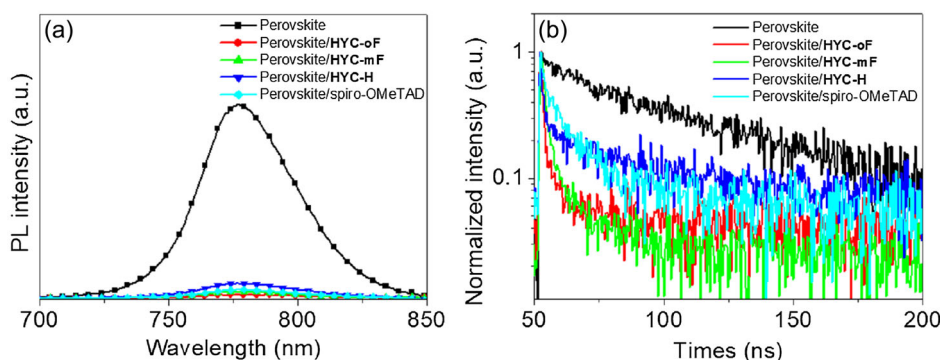


Figure 4. a) Steady-state photoluminescence spectra and b) time-resolved photoluminescence (TRPL) spectra of bare perovskite film, perovskite/HYC-oF, perovskite/HYC-mF, and perovskite/HYC-H films.

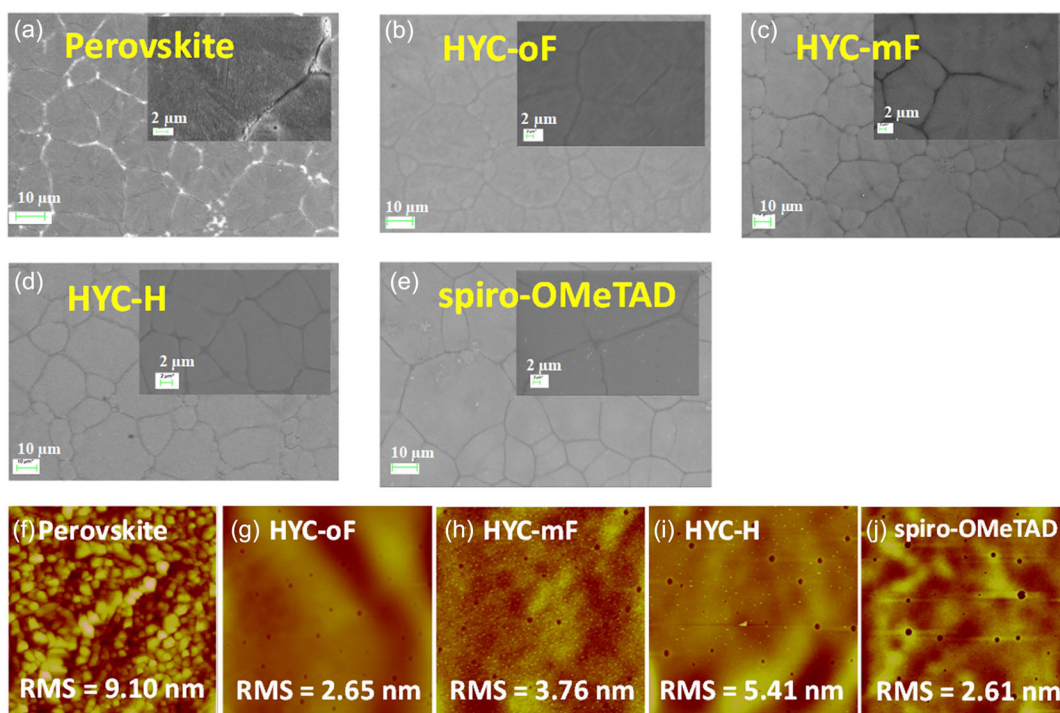


Figure 5. The top-view SEM images a–e) and AFM micrograms f–j) of perovskite film and perovskite/HTMs.

of the TABC-based perovskite underlayer were passivated by the HTM cappings as the bright spots at the surface diminished, which not only could prevent current leakage and facilitate charge extraction, but also prevent the direct contact of perovskite layer with electrode, moisture, and oxygen. In addition, atomic force microscope (AFM) was applied to characterize the surface roughness of HTM films. As shown in Figure 5f–j, the fluorinated HTMs exhibited a lower root-mean-square (RMS) roughness (HYC-oF = 2.65 nm and HYC-mF = 3.76 nm) than that of the non-fluorinated HYC-H film (5.41 nm), and close to the RMS of spiro-OMeTAD (2.61 nm), in contrast to the pristine perovskite films (RMS = 9.10 nm). The homogeneous and smooth fluorinated HYC films are beneficial to forming excellent interfacial contacts and reducing charge-carrier losses at the

perovskite/HTMs interface, which may benefit the photovoltaic performance.

To explore the interaction between the perovskite film and HYC series, X-ray photoelectron spectroscopy (XPS) was performed. Compared with the pristine perovskite film, the characteristic peaks of Pb 4f and I 3d for HYC-capped perovskite films shifted toward the lower binding energy, indicating the interaction between the HTMs and perovskite surface (Figure 6 and Figure S26, Supporting Information). Meanwhile, the two small Pb⁰ peaks at lower energy (137.1 and 142.0 eV) in the perovskite films completely disappeared after being capped with HYC layer, suggesting that a strong interaction between the HTM layer and perovskite surface, which can efficiently passivate the perovskite surface. Moreover, the S 2p peaks of HYC films exhibited an

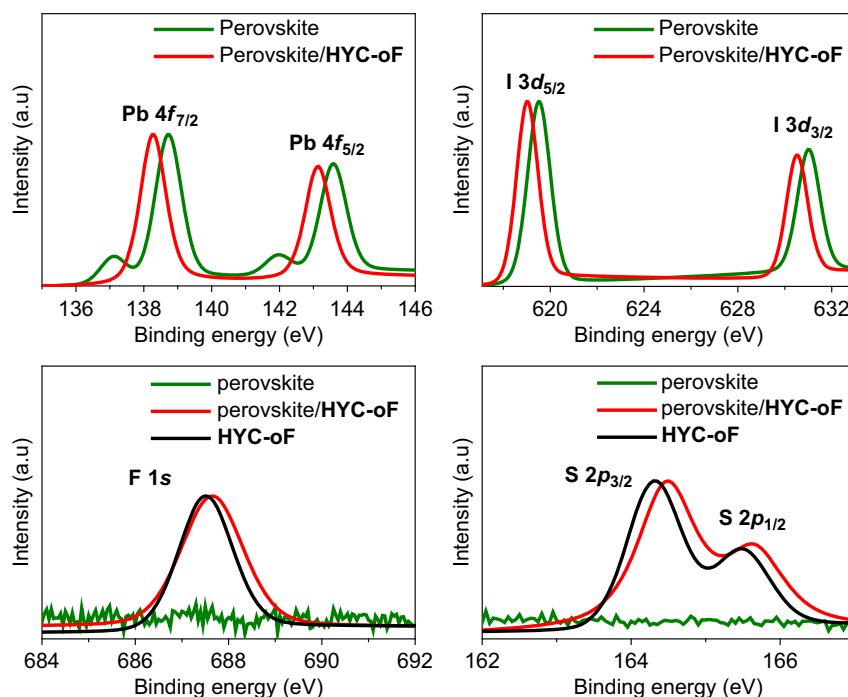


Figure 6. XPS signals of Pb 4f, I 3d, F 1s and S 2p from a pristine HYC-oF film and a HYC-oF coated perovskite film.

opposite shift direction towards higher binding energy after covering the perovskite films, suggesting the existence of Pb-S interaction (Figure 6). In addition, the F 1s peaks of HYC-oF- and HYC-mF films on perovskite shifted toward higher binding energy in comparison with the pristine HYC-oF and HYC-mF film, indicating that fluorinated HTMs can passivate the trap sites of the perovskite film (Figure 6). To further study the interfacial interaction between perovskite film and various HTMs, DFT calculations are applied to calculate the binding energy. As shown in Figure S27, Supporting Information, the binding energies in perovskite/HYC-oF ($-253.95 \text{ kcal mol}^{-1}$) and perovskite/HYC-mF ($-252.12 \text{ kcal mol}^{-1}$) are higher than that of perovskite/HYC-H ($-240.91 \text{ kcal mol}^{-1}$), indicating a tighter packing between the fluorinated HTMs and perovskite film, which may lead to more efficient charge-carrier transfer. We speculate that the increased number of fluorine atoms in HYC-oF and HYC-mF may account for the higher binding energies.

The photovoltaic performance of devices with HYC as HTM is evaluated using the TABC-based perovskite films with a device architecture of FTO/SS c-TiO₂/SS mp-TiO₂/MAPbI₃/HTM/Ag, where the HTM solution is spin-coated on the perovskite layer in a first attempt to investigate the compatibility between TABC-based perovskite film and HYC layers. Meanwhile, the large area c-TiO₂ and mp-TiO₂ layers were prepared by the solution-shearing process (denoted as SS c-TiO₂ and SS m-TiO₂) according to our previous work in order to form the high-quality ETL layers.^[14] The large-area perovskite layer ($10 \times 10 \text{ cm}^2$) was prepared via the TABC method using the optimized process conditions with the precursor solution in acetonitrile/methylamine (ACN/MA) solvent system, where the substrate temperature and

coating speed for the film crystallization were optimized by loading a 120 μL solution at the narrow gap of 250 μm between the moving bar and the ETL substrate. Figure 7a illustrates the TABC process for fabricating perovskite films. The thermal assisted bar-coated large-area ($10 \times 10 \text{ cm}^2$) perovskite film was cut into 37 pieces ($1.5 \times 1.8 \text{ cm}^2$) which are used to prepare small-area (aperture area of 0.04 cm^2) devices. Further details on the device fabrication can be found in the Supporting Information. The digital photograph of the TABC technique is provided in Figure 7b. The energy level diagrams of PSCs and cross-sectional SEM image are illustrated in Figure 7c,d. Figure 7e shows the $J-V$ curves of the optimized devices with HYC series and spiro-OMeTAD as HTM from the reverse scan, with the detailed data collected in Table 2. The HYC-H-based device demonstrated a PCE of 16.98%, with a V_{OC} of 0.99 V, J_{sc} of 22.72 mAcm^{-2} , and FF of 75.47%. As compared with the HYC-H-based device, the fluorinated HYC-oF and HYC-mF devices exhibited better photovoltaic performance. The PCE was improved to 18.38%, along with a V_{OC} of 1.00 V, J_{sc} of 23.50 mAcm^{-2} , and FF of 78.23% when using HYC-mF HTM. In contrast, the PSC with HYC-oF exhibited the best photovoltaic performance, with a PCE of 19.64% with a V_{OC} of 1.01 V, J_{sc} of 24.16 mAcm^{-2} , and FF of 80.52%, which was comparable to the device using spiro-OMeTAD (PCE = 19.02%). The higher PCEs of fluorinated HYC-based (HYC-oF and HYC-mF) devices were mainly attributed to higher hole transporting mobility (Figure S24, Supporting Information), the favorable film morphology (Figure 5), better passivation effect (Figure 6), more suitable energy alignment (Figure 7c), as well as efficient interfacial charge transfer (Figure 4) while comparing with non-fluorinated analogue HYC-H. In addition, the incident photon-to-current

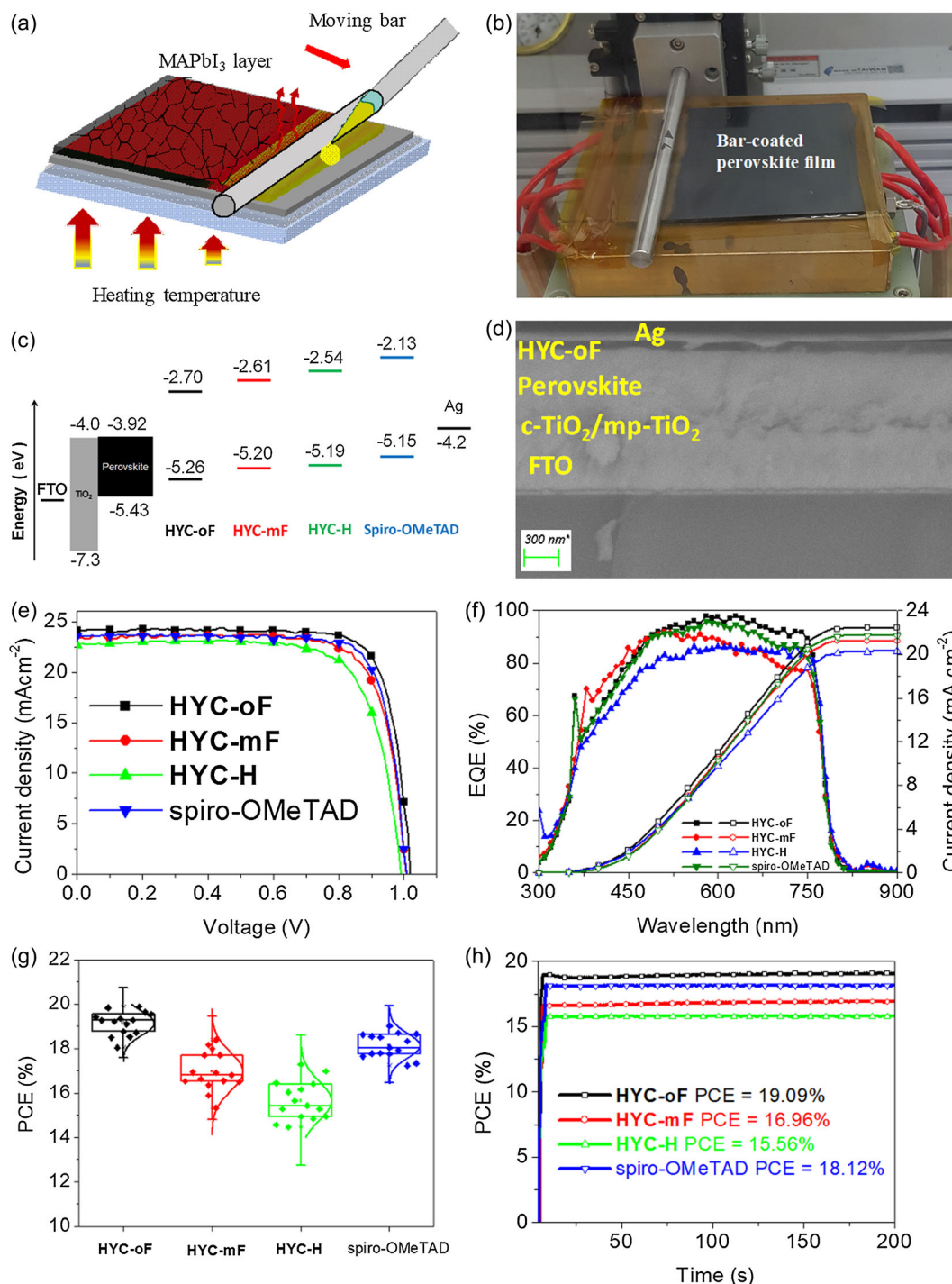


Figure 7. a) Illustration of the overall thermal-assisted bar-coating process. b) Digital photographs of the bar-coated perovskite film. c) Schematic diagram of the device energy level alignment. d) Cross-sectional SEM image of the PSC with **HYC-oF**-based HTM. e) *J*-*V* characteristic of the best-performing PSCs devices with **HYC** series and spiro-OMeTAD as HTMs. f) IPCE spectra and integrated *J*_{sc} curves for the corresponding devices. g) Box chart of PCEs for 15 devices based on **HYC** series and spiro-OMeTAD. h) Steady-state PCE of PSCs with **HYC** series and spiro-OMeTAD under a constant bias of 0.92 V.

efficiency (IPCE) and the integrated *J*_{sc} for the corresponding PSCs were examined. Figure 7f shows the plateau structure in the wavelength ranging between 400 and 760 nm and the integrated *J*_{sc} based on IPCE spectra are estimated to be 22.39,

21.19, 20.30, and 21.68 mAcm⁻² for **HYC-oF**, **HYC-mF**, **HYC-H**, and spiro-OMeTAD, respectively, which are consistent with the measured *J*_{sc}. Moreover, the statistical histograms of the *J*-*V* characteristics of the fabricated PSCs (Figure 7g) displayed

Table 2. Detailed photovoltaic parameters of the PSCs devices based **HYC** series and spiro-OMeTAD as HTMs.

HTM	PCE on Max and Average	V_{oc} [V]	J_{sc} [mA cm^{-2}]	FF [%]	PCE [%]
HYC-oF	max	1.01	24.16	80.52	19.64
	average ^{a)}	1.01 ± 0.01	23.94 ± 0.80	78.93 ± 1.98	19.09 ± 0.49
HYC-mF	max	1.00	23.50	78.23	18.38
	average ^{a)}	1.01 ± 0.01	22.00 ± 1.10	76.21 ± 3.04	16.96 ± 0.83
HYC-H	max	0.99	22.72	75.47	16.98
	average ^{a)}	0.98 ± 0.05	22.09 ± 1.58	72.90 ± 4.36	15.65 ± 0.84
Spiro-OMeTAD	max	1.00	23.61	80.55	19.02
	average ^{a)}	1.01 ± 0.02	23.30 ± 0.78	77.23 ± 2.21	18.12 ± 0.53

^{a)}15 devices were taken to calculate the average values and standard deviations.

average PCE values of 19.09%, 16.96%, 15.65%, and 18.12%, based on **HYC-oF**, **HYC-mF**, **HYC-H**, and spiro-OMeTAD respectively, indicating their excellent reproducibility. The PCEs of 19.38%, 18.01%, 16.52%, and 18.62% for **HYC-oF**-, **HYC-mF**-, **HYC-H**-, and spiro-OMeTAD-based devices were verified the reliability by the steady-state power output (SPO) measured at maximum power point within 200 s (Figure 7h). These results above suggest that the new star-shaped **HYC** HTMs are suitable to be deposited on the TABC-based perovskite films for high efficiency PSCs.

The long-term stability of the unencapsulated devices containing **HYC** series and spiro-OMeTAD as HTMs was assessed in ambient air with $\approx 30\%$ relative humidity (RH). As shown in **Figure 8**, the fluorinated **HYC-oF**- and **HYC-mF**-based devices retained 82% and 79% of the initial PCEs after aging for 720 h. In contrast, the device based on non-fluorinated **HYC-H** decreased to 63% of the original value. Meanwhile, the PSCs with spiro-OMeTAD maintained about 41% of its initial performance. This suggests the device stability is enhanced by the incorporation of fluorine atoms in the molecule. To explore the factor influencing the long-term stability of devices, the hydrophobicity of the HTM films were investigated using water

contact angle measurements. As shown in the inset of Figure 8, the water contact angles of fluorinated **HYC-oF** (110°) and **HYC-mF** (106°) were larger than that of non-fluorinated **HYC-H** (100°) and spiro-OMeTAD (73°), indicating that these fluorinated HTMs are more hydrophobic, which can effectively protect the perovskite film from the humidity. Therefore, the enhanced stability of fluorinated **HYC-oF**- and **HYC-mF**-based devices relative to the non-fluorinated counterpart **HYC-H** can be ascribed to the higher hydrophobicity.

The preliminary evaluation above shows the compatibility of TABC-based perovskite films with fluorinated **HYC-oF** layer for high-performance PSCs. To realize a fully scalable production of PSCs, deposition of **HYC-oF** HTM on perovskite layers by means of the TABC technique was carried out next. The digital photographs of the deposition setup are shown in Figure S28, Supporting Information. **Figure 9a** illustrates the TABC process for coating **HYC-oF** thin layers. A video illustration of the sequential **HYC-oF** coating on top of the perovskite layer is also provided in the Supplementary Information. During this process, the **HYC-oF** solution was dripped in front of the bar and a meniscus formed behind the bar while the bar was moving forward on the perovskite layer. A solid film formed right after the bar passed by. Then, the substrate was annealed to completely evaporate the remained solvent and induce the film formation. The optimized TABC conditions for sequentially coating **HYC-oF** on large-area perovskite layers ($10 \times 10 \text{ cm}^2$) are summarized in Table S19, Supporting Information, and the photographs are shown in Figure 9b. Top-view SEM microgram shows a uniform, pinhole-free, and fully covered surface morphology of **HYC-oF** film was prepared on the large-area perovskite layers (Figure 9b). Further examination of the surface morphology of **HYC-oF**/perovskite blend film by AFM (**Figure 10**) shows that the **HYC-oF** film exhibited a smoother and relatively lower root-mean-square (RMS) roughness (5.42 nm) film than that of spiro-OMeTAD film (RMS = 5.51 nm) by the same process.

With a uniform and dense **HYC-oF** film prepared on perovskite layer all by TABC method, the photovoltaic performance was investigated for PSCs based on such films. Fully scalable PSC with a device architecture of (FTO/SS c-TiO₂/SS mp-TiO₂/MAPbI₃/HTM/Ag), where the ETL (mp-TiO₂/c-TiO₂) was also manufactured by the scalable solution sharing

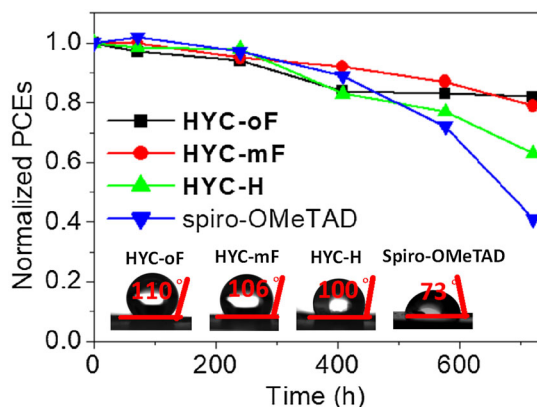


Figure 8. Normalized PCEs of the devices with **HYC** series and spiro-OMeTAD layers. Inset is a water-droplet contact angles on layers of **HYC** series and spiro-OMeTAD.

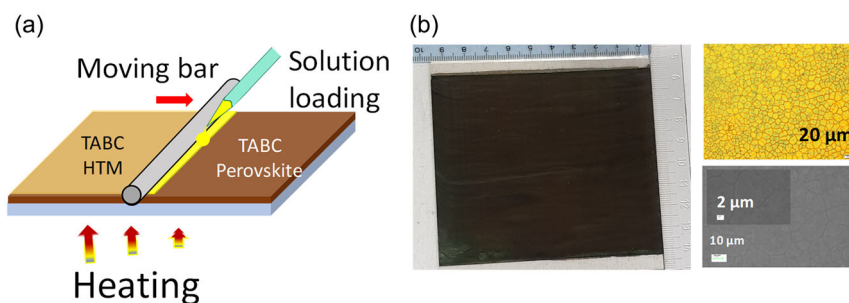


Figure 9. a) Schematic representation of HTM coating via the TABC process. b) Digital photography of bar-coated HYC-oF prepared sequentially with the perovskite underlayer on the large-area (10 cm × 10 cm) substrate and the corresponding SEM images.

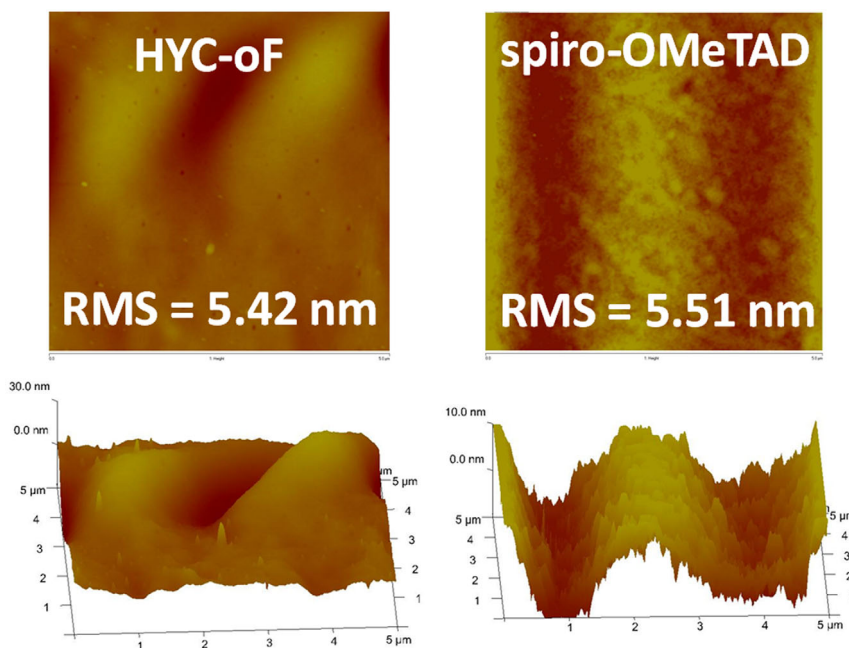


Figure 10. AFM surface and the 3D images of bar-coated HYC-oF and spiro-OMeTAD layers on top of bar-coated perovskite layer (Images were taken in 5 μm × 5 μm area).

method.^[14] Pieces of small area (1.5 × 1.8 cm²) was cut from the large area (10 × 10 cm²) and silver was thermally deposited on top as electrode, with an active area of 0.16 cm², to construct the PSCs. The corresponding devices with TABC-based spiro-OMeTAD were fabricated as control HTM for comparison. A detailed description of device manufacturing can be found in the Supporting Information. **Figure 11a** shows the device structure and the cross-sectional SEM picture of a PSC containing TABC-based HYC-oF HTM with a thickness of ≈150 nm. The *J*-*V* characteristic curves of optimized devices with TABC-based HYC-oF and spiro-OMeTAD as HTMs are shown in **Figure 11b**, and the photovoltaic parameters are listed in **Table 3**. PSCs fabricated with HYC-oF delivered an impressive PCE of 18.49% under reverse scan, together with a *V*_{oc} value of 1.00 V, a *J*_{sc} value of 23.71 mA cm⁻², and a FF of 77.98%. In contrast, the spiro-OMeTAD-based device yielded a lower PCE of 17.51% with a *V*_{oc} of 1.01 V, a *J*_{sc} of 23.58 mA cm⁻², and a FF of 73.51%. Such improved photovoltaic performance is likely to be due to

the better film morphology as well as efficient interfacial charge transfer between the HYC-oF layer and perovskite layer (**Figure 10**), leading to improved *J*_{sc} and FF for HYC-oF-containing PSCs. The IPCE spectra and the corresponding integrated *J*_{sc} are shown in **Figure 11c**. The integrated *J*_{sc} values are 23.42 and 23.25 mAcm⁻² for TABC-based HYC-oF and spiro-OMeTAD, which are in good agreement with the *J*_{sc} values in the *J*-*V* curve. The HYC-oF and spiro-OMeTAD devices also showed a stable power output of 18.01% and 17.12%, respectively at a bias voltage of 0.88 V during 200 s (**Figure S29**, Supporting Information). These results suggest that the promising potential of fluorinated HYC-oF for scalable fabrication of high performance PSCs. To show the film uniformity of TABC-based perovskite and HTM films, the devices made from different areas of the film were prepared and measured. As shown in **Figure 11d**, similar device performance with a maximum PCE of 18.25% and an average PCE of 17.85% were obtained, indicating that the thermal assisted bar-coating process is a promising

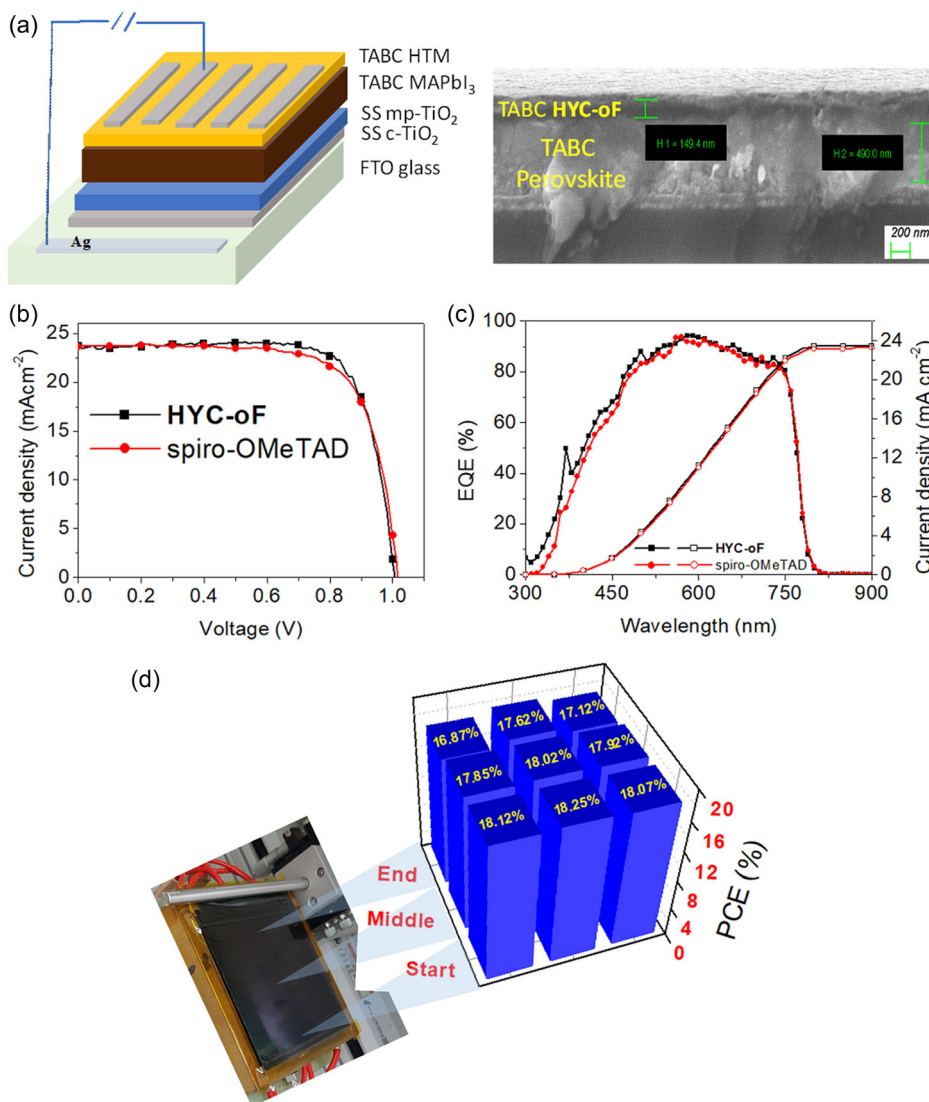


Figure 11. a) Device PSC structure prepared by the scalable process and cross-sectional SEM image of the PSCs. b) J - V curves of PSCs with TABC-based HYC-oF and spiro-OMeTAD. c) IPCE spectra and integrated current density values for the TABC-based HYC-oF and spiro-OMeTAD devices. d) Bar charts showing the PCE distribution of PSCs fabricated on each devices.

Table 3. Photovoltaic performance parameters of HYC-oF and spiro-OMeTAD-based devices fabricated by TABC method.

BC HTM	V_{oc} [V]	J_{sc} [mA [cm] ⁻²]	FF [%]	PCE [%]
HYC-oF	1.00	23.71	77.98	18.49
Spiro-OMeTAD	1.01	23.58	73.51	17.51

technique for obtaining uniform perovskite and HTM films, which is beneficial for high throughput scalable production of PSCs.

3. Conclusions

In conclusion, three novel star-shaped HTMs (HYC-oF, HYC-mF, and HYC-H) with or without fluorine-substituted

triphenylamine unit on CPDT core were designed and synthesized for PSC fabrication. The fluorinated analogues HYC-oF and HYC-mF exhibited suitable energy levels, high hole mobility, improved film quality, enhanced hole extraction/transport ability, higher hydrophobicity, as well as improved passivation effect, compared with those of non-fluorinated HYC-H. In addition, homogeneous and high-quality perovskite films were fabricated on a large scale (10×10 cm) via a simple thermal assisted bar-coating (TABC) method. As a result, the optimized condition for PSCs based on fluorinated HYC-oF and HYC-mF achieved the better PCEs of 19.64% and 18.38%, respectively in comparison with the 16.98% PCE from non-fluorinated counterpart HYC-H when spin-coated on the top of TABC-based perovskite layer. Moreover, PSCs using fluorinated HYC-oF and HYC-mF as HTMs showed improved long-term durability by maintaining about 80% of the initial performance after

720 h under ambient air with $\approx 30\%$ relative humidity (RH). Furthermore, the H₂C-OF was used to demonstrate its potential in fully scalable process of PSC fabrication. We showed that the TABC process can produce a smooth and uniform H₂C-OF layer over a large area TABC-based perovskite films. Thus the PSCs fabricated with H₂C-OF as HTM using the scalable TABC method exhibited an excellent PCE of 18.49%, which is higher than that of spiro-OMeTAD-based PSCs with a PCE of 17.51% under the same fabricating condition. This work proved that the fluorination of star-shaped CPDT-based molecules has a promising application in designing efficient and stable HTMs and can be used for fabricating PSCs by fully scalable process, which is important for the commercialization of PSCs.

Supporting Information

Supporting Information is available from the Wiley Online Library or from the author.

Acknowledgments

G.B.A. and K.-M.L. contributed equally to this work.

Conflict of Interest

The authors declare no conflict of interest.

Data Availability Statement

The data that support the findings of this study are available in the supplementary material of this article.

Keywords

bar coating, cyclopenta[2,1-b₃,4-b']dithiophene, hole-transporting materials, perovskite solar cell

Received: November 29, 2023

Revised: January 9, 2024

Published online:

- [1] a) A. Kojima, K. Teshima, Y. Shirai, T. Miyasaka, *J. Am. Chem. Soc.* **2009**, *131*, 6050; b) Best Research-Cell Efficiency Chart, <https://www.nrel.gov/pv/assets/pdfs/best-researchcell-efficiencies.pdf> (accessed: November 2023). c) H. Min, D. Y. Lee, J. Kim, G. Kim, K. S. Lee, J. Kim, M. J. Paik, Y. K. Kim, K. S. Kim, M. G. Kim, T. J. Shin, S. Il Seok, *Nature* **2021**, *598*, 444. d) R. Lin, J. Xu, M. Wei, Y. Wang, Z. Qin, Z. Liu, J. Wu, K. Xiao, B. Chen, S. M. Park, G. Chen, H. R. Atapattu, K. R. Graham, J. Xu, J. Zhu, L. Li, C. Zhang, E. H. Sargent, H. Tan, *Nature* **2022**, *603*, 73.
- [2] a) J. Cao, F. Du, L. Yang, W. Tang, *J. Mater. Chem. A* **2020**, *8*, 22572; b) Y. Geng, A. Tang, K. Tajima, Q. Zeng, E. Zhou, *J. Mater. Chem. A* **2019**, *7*, 64; c) Z. Wang, S. Yan, Z. Yang, Y. Zou, J. Chen, C. Xu, P. Mao, S. Ding, J. Chen, X. Zong, T. Qin, M. Liang, *Chem. Eng. J.* **2022**, *450*, 138189; d) Y. Wang, W. Chen, L. Wang, B. Tu, T. Chen, B. Liu, K. Yang, C. W. Koh, X. Zhang, H. Sun, G. Chen, X. Feng, H. Y. Woo, A. B. Djurišić, Z. He, X. Guo, *Adv. Mater.* **2019**, *31*, 1902781; e) Y. Chen, X. Xu, N. Cai, S. Qian, R. Luo, Y. Huo, S. W. Tsang, *Adv. Energy Mater.* **2019**, *9*, 1901268.
- [3] J. Cao, Y. M. Liu, X. J. Jing, J. Yin, J. Li, B. Xu, Y. Z. Tan, N. F. Zheng, *J. Am. Chem. Soc.* **2015**, *137*, 10914.
- [4] a) M. Franckevicius, A. Mishra, F. Kreuzer, J. Luo, S.M. Zakeeruddin, M. Gätzel, *Mater. Horiz.* **2015**, *2*, 613; b) S. Ma, H. Zhang, N. Zhao, Y. Cheng, M. Wang, Y. Shen, G. Tu, *J. Mater. Chem. A* **2015**, *3*, 12139; c) M. Saliba, S. Orlandi, T. Matsui, S. Aghazada, M. Cavazzini, J.-P. Correa-Baena, P. Gao, R. Scopelliti, E. Mosconi, K.-H. Dahmen, F. De Angelis, A. Abate, A. Hagfeldt, G. Pozzi, M. Graetzel, M.K. Nazeeruddin, *Nat. Energy* **2016**, *1*, 15017; d) C. Zhou, X. Xu, Z. Liu, Z. Sun, Z. Chen, X. Chen, L. Chen, X. Fang, J. Zhang, Y. M. Yang, X. Jia, N. Yuan, J. Ding, *ACS Appl. Mater. Interfaces* **2023**, *15*, 22752.
- [5] a) Y.-D. Lin, K.-M. Lee, B.-Y. Ke, K.-S. Chen, H.-C. Cheng, W.-J. Lin, S. H. Chang, C.-G. Wu, M.-C. Kuo, H.-C. Chung, C.-C. Chou, H.-Y. Chen, K.-L. Liao, T. J. Chow, S.-S. Sun, *Energy Technol.* **2019**, *7*, 307; b) Y.-D. Lin, S. Y. Abate, H.-C. Chung, K.-L. Liao, Y.-T. Tao, T. J. Chow, S.-S. Sun, *ACS Appl. Energy Mater.* **2019**, *2*, 7070; c) K.-M. Lee, K.-S. Chen, J.-R. Wu, Y.-D. Lin, S.-M. Yu, S. H. Chang, *Nanoscale* **2018**, *10*, 17699; d) Y.-D. Lin, K.-M. Lee, S. H. Chang, T.-Y. Tsai, H.-C. Chung, C.-C. Chou, H.-Y. Chen, T. J. Chow, *ACS Appl. Energy Mater.* **2021**, *4*, 4719; e) K.-M. Lee, W.-H. Chiu, Y.-H. Tsai, C.-S. Wang, Y. T. Tao, Y.-D. Lin, *Chem. Eng. J.* **2022**, *407*, 131609; f) K.-M. Lee, J.-Y. Yang, P.-S. Lai, K.-J. Luo, T.-Y. Yang, K.-L. Liao, S. Y. Abate, Y.-D. Lin, *Chem. Commun.* **2021**, *57*, 6444; g) K.-M. Lee, S. Y. Abate, J. H. Yang, W.-H. Chiu, S. Ahn, S.-R. Li, K.-L. Liao, Y. T. Tao, Y.-D. Lin, *Chem. Eng. J.* **2023**, *454*, 139926; h) K.-M. Lee, Y.-S. Huang, W.-H. Chiu, Y.-K. Huang, G. Chen, G. B. Adugna, S.-R. Li, F.-J. Lin, S.-I. Lu, H.-C. Hsieh, K.-L. Liao, C.-C. Huang, Y. Tai, Y. T. Tao, Y.-D. Lin, *Adv. Funct. Mater.* **2023**, *33*, 2306367.
- [6] a) G. Liu, C. Weng, P. Yin, S. Tan, P. Shen, *Polymer* **2017**, *125*, 217; b) J. Park, E. Jung, J. Jung, W. Jo, *Adv. Mater.* **2013**, *25*, 2583; c) Q. Zhang, M. Kelly, N. Bauer, W. You, *Acc. Chem. Res.* **2017**, *50*, 2401.
- [7] a) Z. Li, Y. Tong, J. Ren, Q. Sun, Y. Tian, Y. Cui, H. Wang, Y. Hao, C.-S. Lee, *Chem. Eng. J.* **2020**, *402*, 125923; b) J. Ren, J. Qu, J. Chen, Z. Li, Q. Sun, H. Wang, Z. Yu, Y. Hao, *J. Power Sources* **2018**, *401*, 29.
- [8] M. Jeong, I. W. Choi, E. M. Go, Y. Cho, M. Kim, B. Lee, S. Jeong, Y. Jo, H. W. Choi, J. Lee, J.-H. Bae, S. K. Kwak, D. S. Kim, C. Yang, *Science* **2020**, *369*, 1615.
- [9] a) N.-G. Park, K. Zhu, *Nat. Rev. Mater.* **2020**, *5*, 333; b) H. Li, J. Zhou, L. Tan, M. Li, C. Jiang, S. Wang, X. Zhao, Y. Liu, Y. Zhang, Y. Ye, W. Tress, C. Yi, *Sci. Adv.* **2022**, *8*, eabo7422; c) G. Tong, D. Son, L. K. Ono, Y. Liu, Y. Hu, H. Zhang, A. Jamshaid, L. Qiu, Z. Liu, Y. Qi, *Adv. Energy Mater.* **2021**, *11*, 2003712; d) Z. Yang, W. Zhang, S. Wu, H. Zhu, Z. Liu, Z. Liu, Z. Jiang, R. Chen, J. Zhou, Q. Lu, Z. Xiao, L. Shi, H. Chen, L. K. Ono, S. Zhang, Y. Zhang, Y. Qi, L. Han, W. Chen, *Sci. Adv.* **2021**, *7*, eabg3749; e) J. Li, J. Dagar, O. Shargaieva, M. A. Flatken, H. Köbler, M. Fenske, C. Schultz, B. Stegemann, J. Just, D. M. Többsen, A. Abate, R. Munir, E. Unger, *Adv. Energy Mater.* **2021**, *11*, 2003460; f) Y. Deng, X. Zheng, Y. Bai, Q. Wang, J. Zhao, J. Huang, *Nat. Energy* **2018**, *3*, 560; g) P. W. Fong, H. Hu, Z. Ren, K. Liu, L. Cui, T. Bi, Q. Liang, Z. Wu, J. Hao, G. Li, *Adv. Sci.* **2021**, *8*, 2003359.
- [10] L. Qiu, S. He, L. K. Ono, S. Liu, Y. Qi, *ACS Energy Lett.* **2019**, *4*, 2147.
- [11] a) M. Han, J. Byeon, J. Jang, C. Hur, G. Seo, M. Choi, *Small Sci.* **2023**, *3*, 2300069; b) D.-N. Jeong, D.-K. Lee, S. Seo, S. Y. Lim, Y. Zhang, H. Shin, H. Cheong, N.-G. Park, *ACS Energy Lett.* **2019**, *4*, 1189; c) J. W. Yoo, J. Jang, U. Kim, Y. Lee, S.-G. Ji, E. Noh, S. Hong, M. Choi, S. Il Seok, *Joule*, **2021**, *5*, 2420. d) K.-S. Lim, D.-K. Lee, J.-W. Lee, N.-G. Park, *J. Mater. Chem. A*, **2020**, *8*, 9345.

- [12] H. D. Pham, T. T. Do, J. Kim, C. Charbonneau, S. Manzhos, K. Feron, W. C. Tsoi, J. R. Durrant, S. M. Jain, P. Sonar, *Adv. Energy Mater.* **2018**, *8*, 1703007
- [13] Y. He, N. Li, T. Heumüller, J. Wortmann, B. Hanisch, A. Aubele, S. Lucas, G. Feng, X. Jiang, W. Li, P. Bäuerle, C. J. Brabec, *Joule* **2022**, *6*, 1160.
- [14] a) G. B. Adugna, S. Y. Abate, W. T. Wu, Y. T. Tao, *ACS Appl. Mater. Interfaces* **2021**, *13*, 25926. b) G. Belay Adugna, S. Yimer Abate, Y.-T. Tao, *Chem. Eng. J.* **2022**, *437*, 135477.
- [15] a) Z. A. Li, Z. L. Zhu, C. C. Chueh, S. B. Jo, J. D. Luo, S. H. Jang, A. K. Y. Jen, *J. Am. Chem. Soc.* **2016**, *138*, 11833; b) P. Xu, P. Liu, Y. Li, B. Xu, L. Kloo, L. Sun, Y. Hua, *ACS Appl. Mater. Interfaces* **2018**, *10*, 19697; c) H. Zhang, Y. Wu, W. Zhang, E. Li, C. Shen, H. Jiang, H. Tian, W.-H. Zhu, *Chem. Sci.* **2018**, *9*, 5919; d) S. A. Ok, B. Jo, S. Somasundaram, H. J. Woo, D. W. Lee, Z. Li, B. G. Kim, J. H. Kim, Y. J. Song, T. K. Ahn, S. Park, H. J. Park, *Nat. Commun.* **2018**, *9*, 4537.